Phys. Status Solidi B **252,** No. 10, 2245–2258 (2015) / **DOI** 10.1002/pssb.201552143

physica status solidi b
www.pss-b.com
basic solid state physics

Crystal and local atomic structure of $MgFeBO_4$, $Mg_{0.5}Co_{0.5}FeBO_4$, and $CoFeBO_4$: Effects of Co substitution

N. V. Kazak[*,1], M. S. Platunov[,1], Yu. V. Knyazev[2], N. B. Ivanova[2], Y. V. Zubavichus[3], A. A. Veligzhanin[3], A. D. Vasiliev[1,2], L. N. Bezmaternykh[1], O. A. Bayukov[1], A. Arauzo[4], J. Bartolomé[5], K. V. Lamonova[6], and S. G. Ovchinnikov[1,2]**

[1] Kirensky Institute of Physics, 660036 Krasnoyarsk, Russia
[2] Siberian Federal University, 660074 Krasnoyarsk, Russia
[3] National Research Center "Kurchatov Institute", 123182 Moscow, Russia
[4] Servicio de Medidas Físicas, Universidad de Zaragoza, 50009 Zaragoza, Spain
[5] Departamento de Física de la Materia Condensada, Instituto de Ciencia de Materiales de Aragón, CSIC, Universidad de Zaragoza, 50009 Zaragoza, Spain
[6] O. O. Galkin Institute for Physics and Engineering, National Academy of Sciences of Ukraine, 83114 Donetsk, Ukraine

Received 17 March 2015, revised 10 May 2015, accepted 3 June 2015
Published online 13 July 2015

Keywords crystal structure, XANES/EXAFS, magnetic semiconductor, oxyborate

[*] Corresponding author: e-mail nat@iph.krasn.ru, Phone: +7 391 249 4556, Fax: +7 391 243 8923
[**] e-mail platunov@iph.krasn.ru, Phone: +7 391 249 4556, Fax: +7 391 243 8923

Single-crystalline $MgFeBO_4$, $Mg_{0.5}Co_{0.5}FeBO_4$, and $CoFeBO_4$ have been grown by the flux method. The samples have been characterized by X-ray spectral analysis, X-ray diffraction, and X-ray absorption spectroscopy. The X-ray absorption near-edge structure (XANES) and extended X-ray absorption fine structure (EXAFS) spectra have been measured at the Fe and Co *K*-edges over a wide temperature range (6.5–300 K). The composition, the charge state, and local environment of both Fe and Co atoms have been determined. The effects of Co substitution for Mg on the local structural distortions have been revealed experimentally and the M–O bond anisotropy has been found.

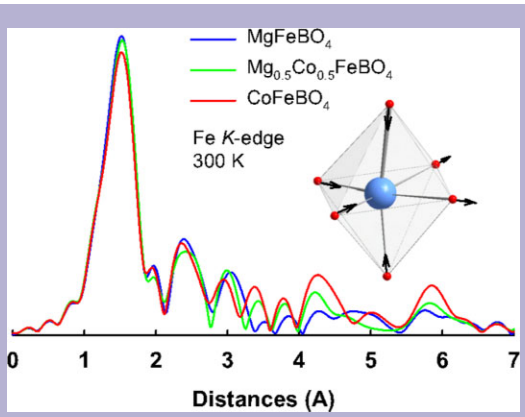

1 Introduction The spectroscopic, magnetic, and electronic properties of the oxyborates remain the focus of numerous studies [1–6]. Special interest is connected with the oxyborates containing transition and the rare-earth metals. The quasilow-dimensionality, magnetic anisotropy, charge and orbital ordering, spin crossover, etc. are believed to be the consequences of strong electron correlation and interrelation between spin and orbital degrees of freedom [7, 8]. The resistive switching found in homometallic Fe_2BO_4 has technological interest for implementation in electronic devices [9]. Quantum entanglement observed in low-dimensional oxyborates has attracted a lot of interest because it is the central resource for applications such as quantum communication and computation [10].

The warwickites $M^{2+}M^{3+}BO_4$ have been a matter of deep study in the past [9, 11] and recently in the search for strongly correlated systems undergoing charge ordering phase transitions [12, 13]. The crystal structure belongs to either orthorhombic or monoclinic system. The former is attributed to a stretching of an octahedral M–O–M axis,

typical of Jahn–Teller (JT) distortion of the metal ion. The structure can be described as an assembly of infinite ribbons extended along the *c*-axis [14]. The ribbons are formed by four chains of edge-sharing oxygen octahedra linked in a 2–1–1–2 sequence, where 1 and 2 denote crystallographically nonequivalent metal sites. It is the trigonal borate group BO_3 responsible for the bonding between ribbons that is the most strongly bonded group of ions in the entire structure.

A variety of heterometallic warwickites has been synthesized to date; $MgGaBO_4$ [15], $MgFeBO_4$ [14], $MgVBO_4$ [14], $MgCrBO_4$ [14], $CoFeBO_4$ [14, 16], $CoCrBO_4$ [15], $NiFeBO_4$ [17], $Fe_{1.91}V_{0.09}BO_4$ [18], $CaInBO_4$ [19] are just some representative examples. An important feature of mixed-metal warwickites is the random distribution of metal ions among nonequivalent metal sites giving rise to random short-range AF interactions. It has been found that heterometallic warwickites ($M^{2+} \neq M^{3+}$) are usually spin glasses with a relatively low temperature T_{SG} of the magnetic transition [20, 21].

The heterometallic $Mg_{1-x}Co_xFeBO_4$ compounds, which behave as spin glasses, with a low transition temperature T_{SG} that increases with Co substitution. They offer the opportunity to study the effect of Co substitution on the structural, electric, and magnetic properties in a regular lattice that has chemical disorder. In contrast to $MgFeBO_4$, which is magnetically isotropic [22], Co may induce anisotropy and modify the spin-glass behavior. In a recent Mössbauer spectroscopic (MS) study as a function of temperature [23], we have found spin-glass behavior in $MgFeBO_4$ and $CoFeBO_4$, with different dynamics near T_{SG}. The increased magnetocrystaline anisotropy by Co substitution increases the magnetic viscosity of the magnetic lattice by freezing magnetic fluctuations below T_{SG}. The low temperature MS spectra analysis also indicates that Fe^{3+} ions have preferential occupation at the M1 site in $MgFeBO_4$ and at M2 sites in $CoFeBO_4$ compounds. In contrast, the electrical transport properties of the compounds do not show a significant dependence on Co content; i.e., in the three compounds with $x = 0$, 0.5 and 1.0, the electrical conduction was found to be governed by Mott variable range hopping at low temperatures (210–270 K) and by thermal activation at high temperatures (280–400 K) [24]. Moreover, magnetization and susceptibility measurements as a function of temperature, field, and relaxation time indicate peculiar spin-glass behavior and quantum entanglement [22]. It is evident from these antecedents that the understanding of the structural details of these compounds, the chemical disorder as a function of Co substitution, and valence distribution are essential to interpret quantitatively the rich phenomenology of the physical properties of these series.

In homometallic compounds, the situation is more complicated. Only two homometallic warwickites, Fe_2BO_4 and Mn_2BO_4, have been reliably characterized so far. Both are mixed-valent compounds and demonstrate magnetic, structural, and charge ordering transitions [25–31]. In addition, the relationship of the electronic and crystal structures in two phases of the Fe_2BO_4 has been assessed, and compared to the V-doped sample where no charge ordering or structural phase transitions take place in a theoretical work [32].

Previous investigations on the bimetallic warwickites dealt with structural and magnetic properties of the compounds where different kinds of metal ions were taken in a 1:1 ratio. The crystal-structure studies were mainly restricted to room-temperature data. The occupation habit of the nonequivalent sites by the different magnetic or nonmagnetic metal atoms may have a bearing on the magnetic properties of these heterometallic spin glasses. An objective of this paper is to elucidate whether there is occupation preference of the Fe and Co atoms upon Co substitution for Mg. Thus, the present work is the study of the crystal and local atomic structure around the iron and cobalt atoms in $Mg_{1-x}Co_xFeBO_4$ warwickite system as a function of temperature (XAS) and Co content (crystallography, XAS). The study includes a detailed structure and electronic state analysis using X-ray single-crystal diffraction. To gain a deeper insight into the valence and coordination state distributions of iron and cobalt ions, XANES and EXAFS experiments at the Fe and Co *K*-edges were conducted. The temperature interval was 6.5–300 K. XANES spectra, in particular pre-edge transitions from 1*s* to unoccupied 3*d* states, give the most valuable information on charge distribution. A comparison of intensities and shifts of exact edge positions with respect to those in reference samples provide qualitative information about the coordination and oxidation states of the metal ions [33, 34]. EXAFS spectra provide element-specific local structure parameters [35].

With this respect, the purpose of the present study is to clarify the effects of Co addition on the crystal structure, electronic state and local structure distortions, in conjunction with the variation of the Fe–O and Co–O bond lengths within the FeO_6 and CoO_6 octahedra.

2 Experimental procedure Single crystals of Mg–Fe, Mg–Co–Fe, and Co–Fe warwickites were grown by the flux method in the system $Bi_2Mo_3O_{12}$–B_2O_3–CoO–MgO–Fe_2O_3. The saturation temperature was $T_{sat} \leq 980\,^{\circ}C$ and the crystallization interval was $\Delta T_{cr} \geq 30\,^{\circ}C$. The flux was heated at 1050 °C during 4–6 h and then fast cooled to $T \approx T_{sat}$–(10 to 12) °C and subsequently slowly cooled at a rate of 4–6 °C/day. The growing process was continued for 3 days. Then, the product was subjected to etching in 20% aqueous nitric acid. Needle-shaped black crystals with a typical size of $0.5 \times 0.2 \times 5.0\,mm^3$ were obtained.

Extremely high-purity specimens have been prepared; the composition study was carried out by X-ray spectral analysis using scanning electron-probe microanalyzer (SEPMA) JEOL JXA-8100. The wavelength-dispersive method was used, operating at 15 kV accelerating voltage, 30 nA sample current, 2–4 μm beam diameter, and 10 s counting time on peak and 5 s on backgrounds. Natural minerals (Fe_2O_3, MgO, CoO, B_2O_3) were used as standards.

Prior to characterization, the samples were polished. The analysis was performed from 20 arbitrarily chosen points across the sample surface. All Fe content was postulated to be Fe^{3+}, while Co was assumed to be Co^{2+}. The determination of element concentrations was carried out by the ZAF quantification procedure. The obtained results show that strict stoichiometry is preserved for all samples. For Mg–Fe warwickites, the ionic ratio Mg/Fe was 0.94/1.06; therefore, below we shall use the chemical formula $MgFeBO_4$. For Co–Fe warwickite, the ionic ratio Co/Fe was found to be 0.97/1.03 and the chemical formula is $CoFeBO_4$. In the Mg–Co–Fe warwickite, the content of Mg and Co was found to be approximately equal and half of the Fe content, so we formulate this sample as $Mg_{0.5}Co_{0.5}FeBO_4$.

An X-ray crystallographic study was carried out with a SMART APEX II diffractometer with graphite-monochromatic MoKα radiation. The SHELXL-97 [36] software package was used to solve the structure and refine it with the full-matrix least-*k* squares method on F^2.

The XAS measurements were performed at the Structural Materials Science beamline of the National Research Center "Kurchatov Institute" (Moscow) in the transmission mode. XAS measurements were carried out at temperatures ranging from 6.5 to 300 K using a SHI closed-cycle helium refrigerator (Japan). The storage ring operated at an electron energy of 2.5 GeV and an average electron current of about 80 mA. For the selection of the primary beam photon energy, a Si (111) channel-cut monochromator was employed, which provided an energy resolution $\Delta E/E \sim 2 \times 10^{-4}$. Primary and transmitted intensities were recorded using two independent ionization chambers filled with appropriate N_2/Ar mixtures. The energy was calibrated using corresponding metal foils.

The EXAFS spectra were collected at the Fe and Co K absorption edges using optimized scan parameters of the beamline software. The ΔE scanning step in the XANES region was about 0.5 eV, and scanning in the EXAFS region was carried out at a constant step on the photoelectron wave number scale with $\Delta k = 0.05$ Å^{-1}, giving an energy step of the order of 1.5 eV. Single-crystalline samples for XAS measurements were ground to fine powders and then spread uniformly onto a thin adhesive kapton film and folded into several layers to give an absorption edge jump around unity.

The EXAFS spectra $\mu(E)$ were normalized to an edge jump and the absorption coefficient of the isolated atoms $\mu_0(E)$ was extracted by fitting a cubic spline function to the data. After subtraction of the atomic background, the conversion from E to k scale was performed. Structural parameters for the starting model were taken from the X-ray single-crystal diffraction analysis. The k^3-weighted EXAFS function $\chi(k)$ was calculated in the intervals $k =$ 2–15.3 Å^{-1} ($CoFeBO_4$) and $k =$ 2–12.2 Å^{-1} ($MgFeBO_4$ and $Mg_{0.5}Co_{0.5}FeBO_4$) using a Kaiser–Bessel window (local order peaks were clearly distinguishable against the background up to 7 Å). The EXAFS structural analysis was performed using theoretical phases and amplitudes as calculated by the FEFF-8 package [37], and fits to the experimental data were carried out in *R*-space with the IFFEFIT package [38]. EXAFS analysis of the warwickite systems remains complicated due to the presence of two nonequivalent metal sites in the crystal structure giving rise to strongly overlapped contributions of coordination shells. Therefore, the EXAFS analysis is restricted to the first oxygen shell M–O.

3 Results and discussion

3.1 X-ray diffraction The crystallographic data for Mg–Fe, Mg–Co–Fe, and Co–Fe warwickites are summarized in Tables 1 and 2, and in S1 of Supporting Information (Crystal and local atomic structure of Co-doped $MgFeBO_4$ warwickites). The compounds crystallize in an orthorhombic system. The lattice parameters vary linearly as the cobalt content increases (thus obeying the Vegard's law). The *c* parameter increases, while *a* and *b* decrease. All parameters are in good agreement with those reported earlier [14]. The metal ions occupy two nonequivalent crystallographic sites both belonging to general 4*c* Wyckoff positions. These positions are indicated as M1 and M2 (see Fig. 1). The boron ions reside in only one position and O ions are distributed among four distinct positions.

The general features of the crystal structure are typical for warwickites [39]: the metal ions are surrounded by oxygen octahedra. These octahedra are linked by sharing their edges, thus forming four octahedra flat ribbons extending along the *c*-axis (Fig. 2). The row consisting of four octahedra stacked in the sequence 2–1–1–2 is located across the ribbon. The coordination octahedra around the M2 position form the outer columns of the ribbon and the octahedra around the M1 position form the inner two columns. The planar trigonal borate group (BO_3) located in the voids between the ribbons are attached to them by corner sharing. The mean B–O bond length and the mean O–B–O bond angle are in a good agreement with a trigonal planar geometry in all samples.

The octahedron $M1O_6$ is smaller than $M2O_6$ in the Mg–Fe and the Mg–Co–Fe warwickites, as deduced from the average M–O distances (Table 2). As the Co content increases, the average M–O bond distances vary. The M1–O bond distance increases, while the M2–O bond distance decreases. As a consequence, the $M1O_6$ octahedron becomes larger than $M2O_6$ ones in the Co–Fe warwickite. The shorter M–O distances provide stronger 3D repulsion and lead to apparently increased oxidation state. It means that trivalent Fe ions would prefer to occupy the smaller octahedra $M1O_6$ in the Mg–Fe and Mg–Co–Fe warwickites, while they would reside at the $M2O_6$ octahedra in the Co–Fe warwickite.

The ionic distributions can be studied by the calculation of bond valence sums (BVS) at a specific site $BVS_i = \sum_j \exp(r_0 - r_{ij})/B$, with r_{ij} being the bond length between two atoms; r_0 and B are empirical parameters tabulated in Refs. [40, 41].

Using the parameters for Mg^{2+}, Co^{2+}, Co^{3+}, Fe^{2+}, and Fe^{3+}, the bond valence sums (BVS) for the M1 and M2

Table 1 Crystal data and refinement results for Mg–Fe, Mg–Co–Fe, and Co–Fe warwickites.

	Mg–Fe	Mg–Co–Fe	Co–Fe
formula weight ($g\,mol^{-1}$)	154.97	172.27	189.59
crystal system	orthorhombic	orthorhombic	orthorhombic
space group	*Pnma* (62)	*Pnma* (62)	*Pnma* (62)
unit-cell parameters (Å)			
a	9.2795(10)	9.2449	9.2144
b	9.4225(10)	9.3898	9.3651
c	3.1146(3)	3.1185	3.1202
unit-cell volume ($Å^3$)	272.33(5)	270.71(6)	269.25
Z	4	4	4
calculated density ($g\,cm^{-3}$)	3.78	4.22	4.68
radiation	MoKα	MoKα	MoKα
wavelength λ (Å)	0.71073	0.71073	0.71073
temperature (K)	296	296	296
crystal shape	needle (along *c*)	needle (along *c*)	needle (along *c*)
abs. coefficient (mm^{-1})	2.785	5.764	5.672
F (000)	150	204	180
Θ range (deg)	3.08–29.44	3.09–29.74	3.10–29.75
limiting indices	$-12 \le h \le 12$	$-12 \le h \le 12$	$-12 \le h \le 12$
	$-4 \le k \le 4$	$-4 \le k \le 4$	$-4 \le k \le 4$
	$-12 \le l \le 12$	$-12 \le l \le 12$	$-12 \le l \le 12$
extinction coefficient	0.123(6)	0.125(7)	0.256(14)
data/restraints/parameters	437/0/44	439/0/46	437/0/44
goodness-of-fit on F^2	1.187	1.133	1.223
final *R* indices			
*R*1	0.0187	0.0228	0.0290
w*R*2	0.0459	0.0575	0.0759

positions are listed in Table 3. With the Mg^{2+} and Co^{2+} parameters, the corresponding BVS values lie in the range of 2.14–2.23 and 2.18–2.22 valence units (v.u.), respectively. Usually, bond valence sums contain variations of about 10% even in typical compounds, such as CoO and Co_2O_3, which can be attributed to inaccuracy of the interatomic distances. However, the BVS values for Co^{3+} (~1.89) and Fe^{2+} (~2.46) are very different from the expected values 3 and 2, respectively. Therefore, it can be considered that in the warwickites under investigation, the metal ions correspond to the following charge states: Co and Mg are divalent and Fe is trivalent. The small reduction of the BVS value at the M2 position in comparison with the M1 one in the Mg–Fe and the Mg–Co–Fe samples can be an indication that Mg has a preference for this position (M2).

The sum of the metal ion occupancies at each of two distinct crystallographic positions was fixed to 1. The results of the refinements of the Fe, Co, and Mg occupancies at the M1 and M2 positions are listed in Table 4. In Mg–Fe warwickite, the M1 position can be treated as preferably occupied by Fe ions. The average valences at M1/M2 positions for Mg–Fe warwickite are found to be 2.54/2.26, respectively. This is roughly consistent with the valence distribution in a warwickite (e.g., in Mg–Sc warwickite, the charges are +2.76 and +2.24 for M1 and M2 position, respectively) [42]. The Fe site occupation probability has been determined from Mössbauer spectroscopy independently. They can be compared in Table 4, for $MgFeBO_4$, where a reasonable agreement is found within the experimental error bars, and they are determined for $CoFeBO_4$ [23].

The $M1O_6$ and $M2O_6$ octahedra undergo high-symmetry distortions such as a breathing mode and the low-symmetry rhombic and trigonal distortions. Normal coordinates Q_α ($\alpha = 1, 2, \ldots, 3N-3$; *N* is the number of ligands) are linear combinations of the Cartesian coordinates of oxygen, and classified according to the irreducible representations of the coordination complex symmetry (Tables 5 and S2), in terms of the O_h symmetry group. The Q_1 coordinate describes high-symmetry distortions. The other normal coordinates correspond to low-symmetry distortions like rhombic (or JT, Q_2, and Q_3) and trigonal (Q_4, Q_5, Q_6) ones. The Q_3 coordinate presents tetragonal octahedral distortion along the *z*-axis, whereas the Q_2 ones correspond to the distortions with rhombic symmetry. The metal–oxygen bond lengths are distributed so that four bonds (O3, O4 for M1 site and O2, O1 for M2 one) are roughly coplanar and the two other ones (O2, O4 for M1 and O3, O4 for M2) are axial (see Fig. 1). The JT-like compression can be seen to involve a O2–M1–O4 and O3–M2–O4 axes. There is a stretching of the other two axes, with the largest distances among two M–O bonds (~2.165

Table 2 Selected bond lengths (Å^2) and angles (deg) for Mg–Fe, Mg–Co–Fe, and Co–Fe warwickites.

metal coordination	Mg–Fe	Mg–Co–Fe	Co–Fe
M1–O2	2.0811(14)	2.081(2)	2.083(3)
M1–O4	2.0083(14)	2.005(2)	1.998(3)
M1–O3^{iii}	2.164(1)	2.1566(14)	2.156(2)
M1–O3^{iv}	2.164(1)	2.1566(14)	2.156(2)
M1–O4^{i}	1.993(1)	2.004(1)	2.013(2)
M1–O4^{ii}	1.993(1)	2.004(1)	2.013(2)
⟨M1–O⟩	2.0672	2.0680	2.0698
M2–O3	2.1484(15)	2.128(2)	2.114(3)
M2–O4	1.9989(14)	1.975(2)	1.956(3)
M2–O2^{vii}	2.165(1)	2.1612(14)	2.156(2)
M2–O2^{viii}	2.165(1)	2.1612(14)	2.156(2)
M2–O1^{i}	2.009(1)	2.011(1)	2.013(2)
M2–O1^{ii}	2.009(1)	2.011(1)	2.013(2)
⟨M2–O⟩	2.0825	2.0746	2.0681
O2–M1–O4^{i}	99.25(5)	98.70(6)	98.5(1)
O2–M1–O4^{ii}	99.25(5)	98.70(6)	98.5(1)
O2–M1–O3^{iii}	81.55(5)	81.60(6)	81.59(9)
O2–M1–O3^{iv}	81.55(5)	81.60(6)	81.59(9)
O4–M1–O4^{i}	84.95(5)	85.03(6)	85.2(1)
O4–M1–O4^{ii}	84.95(5)	85.03(6)	85.2(1)
O4–M1–O3^{iii}	93.75(5)	94.28(6)	94.4(1)
O4–M1–O3^{iii}	93.75(5)	94.28(6)	94.4(1)
O2–M1–O4	173.19(6)	173.98(6)	174.2(1)
O4^{i}–M1–O3^{iii}	174.34(5)	175.08(6)	175.5(1)
O4^{ii}–M1–O3^{iv}	174.34(5)	175.08(6)	175.5(1)
O3–M2–O2^{vii}	80.02(5)	80.42(6)	80.89(9)
O3–M2–O2^{viii}	80.02(5)	80.42(6)	80.89(9)
O3–M2–O1^{i}	95.75(5)	94.98(6)	94.1(1)
O3–M2–O1^{ii}	95.75(5)	94.98(6)	94.1(1)
O4–M2–O2^{vii}	93.02(5)	93.13(6)	93.0(1)
O4–M2–O2^{viii}	93.02(5)	93.13(6)	93.0(1)
O4–M2–O1^{i}	90.61(5)	90.93(6)	91.5(1)
O4–M2–O1^{ii}	90.61(5)	90.93(6)	91.5(1)
O3–M2–O4	169.91(6)	170.62(6)	171.1(1)
O2^{viii}–M2–O1^{ii}	174.01(5)	173.88(6)	173.7(1)
O2^{vii}– M2–O1^{i}	174.01(5)	173.88(6)	173.7(1)
boron coordination			
B–O1	1.357(3)	1.353(4)	1.356(6)
B–O2	1.405(2)	1.400(3)	1.388(5)
B–O3^{ix}	1.391(2)	1.388(3)	1.383(5)
⟨B–O⟩	1.384	1.380	1.376
O1–B–O2	119.1(2)	119.1(2)	119.6(4)
O2–B–O3^{ix}	120.2(2)	120.0(3)	120.3(4)
O3^{ix}–B–O1	120.8(2)	120.9(2)	120.1(4)
⟨O–B–O⟩	120	120	120

Upper indexes are symmetry codes: (i) $1-x$, $1-y$, $1-z$; (ii) $1-x$, $1-y$, $-z$; (iii) $0.5-x$, $0.5+y$, $-z$; (iv) $0.5-x$, $0.5+y$, $1-z$; (v) x, y, $1+z$; (vi) x, y, $-1+z$; (vii) $0.5-x$, $-0.5+y$, $-z$; (viii) $0.5-x$, $-0.5+y$, $1-z$; (ix) x, $1+y$, z; (x) x, $-1+y$, z; (xi) $1-x$, $1-y$, $0.5+z$; (xii) $1-x$, $1-y$, $-0.5+z$.

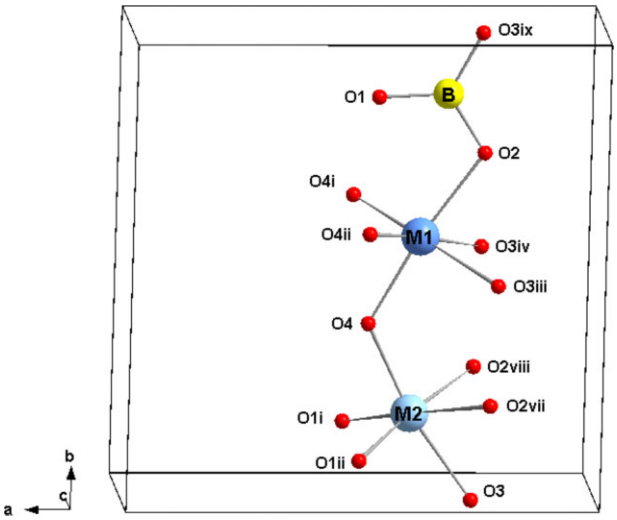

Figure 1 The metal and boron atoms coordination environments. The unit cell is shown.

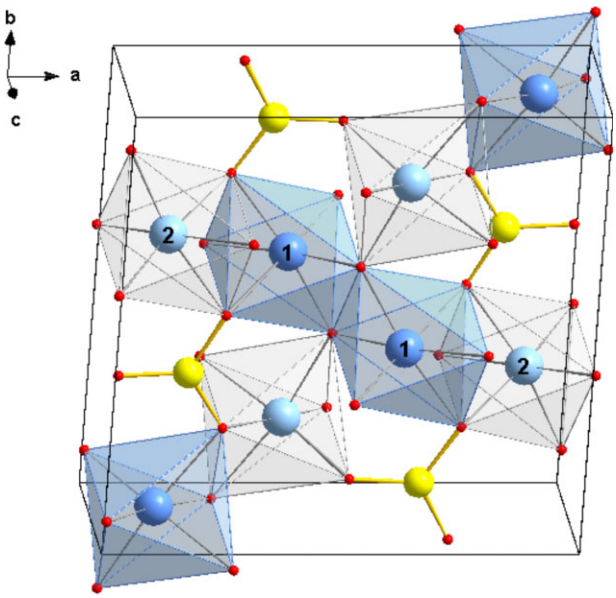

Figure 2 The schematic structure of warwickite. The metal cations have octahedral coordination, where the edge-sharing octahedra form ribbons. Coordination octahedra around the M1 position (labeled 1) are dark and those around the M2 position (labeled 2) are light. The boron atom positions drawn as yellow circles have trigonal coordination. The unit cell and axes directions are shown.

and 2.156 Å for $x=0.0$ and 1.0, respectively). The compression is significant for M1 site in Mg–Fe and for M2 site in Co–Fe, as seen from the planar/axial average radii ratio (2.079/2.045 Å for Mg–Fe) and (2.085/2.035 Å for Co–Fe). In $MgFeBO_4$, the rhombic distortion of the $M2O_6$ octahedra (0.0133 Å) is larger than that of the $M1O_6$ (0.002 Å), while the tetragonal distortion is more pronounced for the $M1O_6$ octahedron (−0.0131 Å). The Co addition gives rise to a rapid decrease in the axial average radius of the $M2O_6$ octahedra (from 2.074 Å for $x=0$ to 2.035 Å for $x=1.0$) as compared to one of the $M1O_6$ ones

Table 3 The estimated empirical bond valence sums for the metal ions (v.u.).

	Mg–Fe		Mg–Co–Fe		Co–Fe	
	M1	M2	M1	M2	M1	M2
Mg^{2+}	2.23	2.14	2.21	2.19		
Co^{2+}			2.21	2.18	2.19	2.22
Co^{3+}			1.90	1.88	1.89	1.91
Fe^{2+}	2.49	2.39	2.47	2.44	2.46	2.49
Fe^{3+}	2.66	2.56	2.65	2.61	2.63	2.66
B^{3+}	2.89		2.93		2.96	

(from 2.045 Å for $x = 0$ to 2.041 Å for $x = 1.0$). This leads to a situation when both types of the low-symmetry distortions (Q_2, Q_3) are prevailing for M2 site for the Co–Fe warwickite. The rhombic distortion of the $M1O_6$ octahedron increases by approximately one order of magnitude as the Co content increases, as can be seen from comparison of the Q_2 coordinates. The tetragonal distortion shows a significant growth for the $M2O_6$ octahedra with an increase in the Co concentration. Thus, the JT-like distortion is expected to increase as the cobalt content increases. In addition, the trigonal distortions are comparable for both oxygen octahedra and are weakly affected by the Co substitution.

We have estimated the octahedral deformation by means of the electric-field gradient (EFG) calculation. The EFG generated by the oxygen octahedron on the metal sites M1 and M2 can be expressed as follows:

$$G_{\alpha\beta} = 2e\sum_i \frac{3\cos^2\varphi_i - 1}{r_i^3},$$

φ_i is the angle between the principal octahedra axis and the direction toward the ith oxygen anion, r_i is the distance between the cation and the ith oxygen anion. The main component (V_{zz}) of the $G_{\alpha\beta}$ tensor for both metal sites are listed in Table 6. The EFG created at M1 in the Mg–Fe warwickite is considerably higher than the one at the M2 site showing that site M1 is ~2.1 times more distorted than site M2. As the Co content increases, the V_{zz} shows a gradual growth for the inner $M1O_6$ and a rapid increase for the outer $M2O_6$ oxygen octahedra. So, from the EFG calculation, we conclude that Co substitution induces an increase in degree of distortion of the coordination octahedra around the metal ions.

Table 4 Site occupation factors (SOF) for the M1 and M2 sites, as determined from X-ray diffraction (XRD) (±1%) and Mössbauer spectroscopy (MS) (the iron occupation factor, ±1.5%, Ref. [23]).

	XRD		MS	
	M1	M2	M1	M2
$MgFeBO_4$	0.72(Fe) + 0.28(Mg)	0.28(Fe) + 0.72(Mg)	0.57(Fe) + 0.43(Mg)	0.41(Fe^{3+}) + 0.02(Fe^{2+}) + 0.57(Mg)
$Mg_{0.5}Co_{0.5}FeBO_4$	0.89(Fe/Co) + 0.11(Mg)	0.65(Fe/Co) + 0.35(Mg)		
$CoFeBO_4$			0.44(Fe^{3+}) + 0.56(Co)	0.54(Fe^{3+}) + 0.02(Fe^{2+}) + 0.44(Co)

Table 5 The ligand's displacement (Å) for metal ions in the $M1O_6$ and $M2O_6$ octahedral complexes. The R_0 is the M–O distance in the undistorted octahedron that is accepted such in order to provide a zero value of Q_1.

normal coordinates	Mg–Fe		Mg–Co–Fe		Co–Fe	
	M1	M2	M1	M2	M1	M2
Q_2	0.002	0.0133	0.0201	0.0143	0.0193	0.0149
Q_3	–0.0131	–0.0088	–0.0169	–0.0319	–0.0249	–0.0496
Q_4	0.2414	0.1761	0.2405	0.1627	0.2388	0.1447
Q_5	0.2407	0.1725	0.2398	0.1594	0.2384	0.1416
Q_6	–0.2893	–0.2534	–0.2896	–0.2597	–0.2833	–0.2633
Q_7	0.0601	–0.0829	0.053	–0.0765	0.0508	–0.0718
Q_8	0.069	–0.0921	0.0608	–0.0854	0.0582	–0.0805
Q_9	–0.026	–0.0576	–0.0163	–0.0645	–0.0132	–0.0710
Q_{10}	0.0479	–0.024	0.0421	–0.0244	0.0384	–0.0238
Q_{11}	0.055	–0.0267	0.0484	–0.0272	0.0441	–0.0266
Q_{12}	0.0459	–0.034	0.0421	–0.0327	0.0451	–0.0319
Q_{13}	0.0077	0.0489	0.0066	0.042	0.0036	0.0382
Q_{13}	–0.0089	–0.0543	–0.0076	–0.0469	–0.0041	–0.0428
Q_{15}	0	0	0	0	0	0

Table 6 The main component V_{zz} of EFG tensor for $M1O_6$ and $M2O_6$ oxygen octahedra (eÅ^3).

	M1	M2
$MgFeBO_4$	0.0928	0.0438
$Mg_{0.5}Co_{0.5}FeBO_4$	0.0954	0.0696
$CoFeBO_4$	0.1040	0.0873

The EFG principal axis lies along the M1–O2 and M2–O3 bonds for the $M1O_6$ and $M2O_6$ octahedra, respectively. The directions of the EFG principal axes are alternated from site to site in the row 2–1–1–2, which indicates that there is inversion of the principal axis for every second ion along the ribbon substructure (Fig. 3).

The main results of the structural study on Mg–Fe, Mg–Co–Fe, and Co–Fe warwickites may be summarized as follows: (i) Co and Mg enter into the warwickite structure in the divalent state, and Fe in the trivalent state; (ii) both (M1 and M2) positions are occupied by a mixture of Mg, Co, and Fe atoms; (iii) the trivalent Fe ions prefer smaller octahedra: $M1O_6$ in the Mg–Fe and Mg–Co–Fe warwickite, and the $M2O_6$ one in the Co–Fe compound; (iv) both octahedra are compressed along one of the nominal fourfold axis and the Co addition increases the octahedral distortion; and (v) the principal axis of the octahedra is inverted for every second metal ion along the ribbon structure.

3.2 X-ray absorption spectroscopy

3.2.1 XANES spectra Figure 4 shows normalized Fe K-edge XANES spectra and their first derivatives of the warwickites under study recorded over a wide temperature range. The FeO and Fe_2O_3 have been used as references for the Fe^{2+} and Fe^{3+} charge states. There is a strong similarity in the spectral line shapes at different temperatures. A weak pre-edge absorption feature (A) at ~7115 eV, followed by a weak shoulder on a rising absorption curve (the absorption edge is at ~7124 eV) that culminates in a strong peak in the vicinity of ~7132 eV (B). This strong peak has been assigned to a dipole-allowed transition 1s–4p and the pre-edge feature just below the threshold as a dipole-forbidden transition 1s–3d, which has a nonzero probability due to a partial p–d mixing and quadrupole contribution. The difference in the energy position of the main absorption edge for the samples and FeO reference can be seen. The main edge position for warwickites is found to be ~3 eV higher than that for Fe^{2+} compounds, as deduced from the maximum of the derivative spectra in Fig. 4b, d, and f, but very close to that of Fe^{3+} compound, thus indicating that the valence state of the Fe is mainly +3. The pre-edge 1s–3d transition probability is related to the coordination symmetry and to the occupancy of the 3d shell of the transition metal. As the iron ions were found to be in the trivalent state, the transition is closely associated with the presence of the local inversion symmetry of the first coordination shell. In an ideal octahedral symmetry, the p–d mixing is symmetry-forbidden. For noncentrosymmetric environments around the Fe ion, i.e., in distorted FeO_6 octahedra, this transition gains some intensity. The weak intensity of the pre-edge feature is in agreement with the six-coordinated Fe being located in relatively weakly distorted sites.

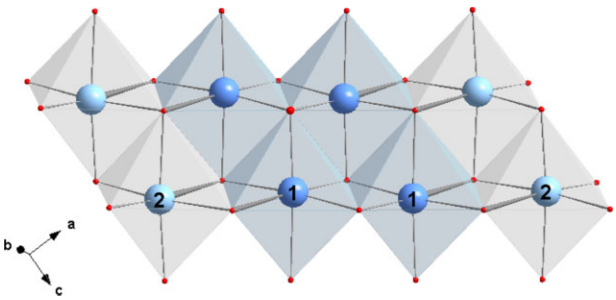

Figure 3 Two 2–1–1–2 rows of the infinite ribbon are shown. The directions of the principal axes of the octahedra $M1O_6$ and $M2O_6$ are highlighted in bold.

The room temperature Fe K-edge spectra of all three samples are plotted in Fig. 5. The curve's behavior is common for all orthorhombic warwickites. As shown in the insets of Fig. 5, the intensity of the peak A experiences no changes, while the intensity of the peak B slightly reduces with increasing Co content. This effect can be explained in terms of the difference in the degree of the orbital mixing which arises from the variation of local structure upon Co doping. The main-edge position is independent of both Co content and temperature. Thus, the XANES results at the Fe K-edge are consistent with the previous finding that Fe ions enter the warwickite structure in the trivalent state predominantly and are located inside the slightly distorted octahedral sites.

The normalized Co K-edges XANES spectra of the Co-containing warwickites measured over a wide temperature range are shown in Fig. 6. Also, the room-temperature spectra of CoO and Co_2O_3 are included as references for the Co^{2+} and Co^{3+} charge states, respectively. The warwickites spectra are characterized by a low-intensity peak at 7709 eV, a shoulder at 7715 eV, and a steeply rising edge (the main absorption edge is at 7719 eV) that leads to a series of well-defined peaks at 7709 (A), 7725 (B), and 7738 eV (C), and to others at higher energy in the EXAFS region. The inflection point associated with each of these features shows up more clearly in the derivative spectrum (bottom panels of Fig. 6). The weak intensity pre-edge peak at ~7709 eV correspond to the 1s–3d absorption process. The main peak (7725 eV) corresponds to the 1s–4p transition. The main edge energy (7719 eV) is very close to that of CoO (7720 eV), but prominently different from that of Co_2O_3 (7727 eV), thus indicating the prevailing divalent state of cobalt. Since there is no shift of the main edge absorption as Co content increases (Fig. 7), we conclude that the valence of cobalt is independent of cobalt content. Both samples exhibit the same intensity in the pre-edge feature at ~7709 eV, and in

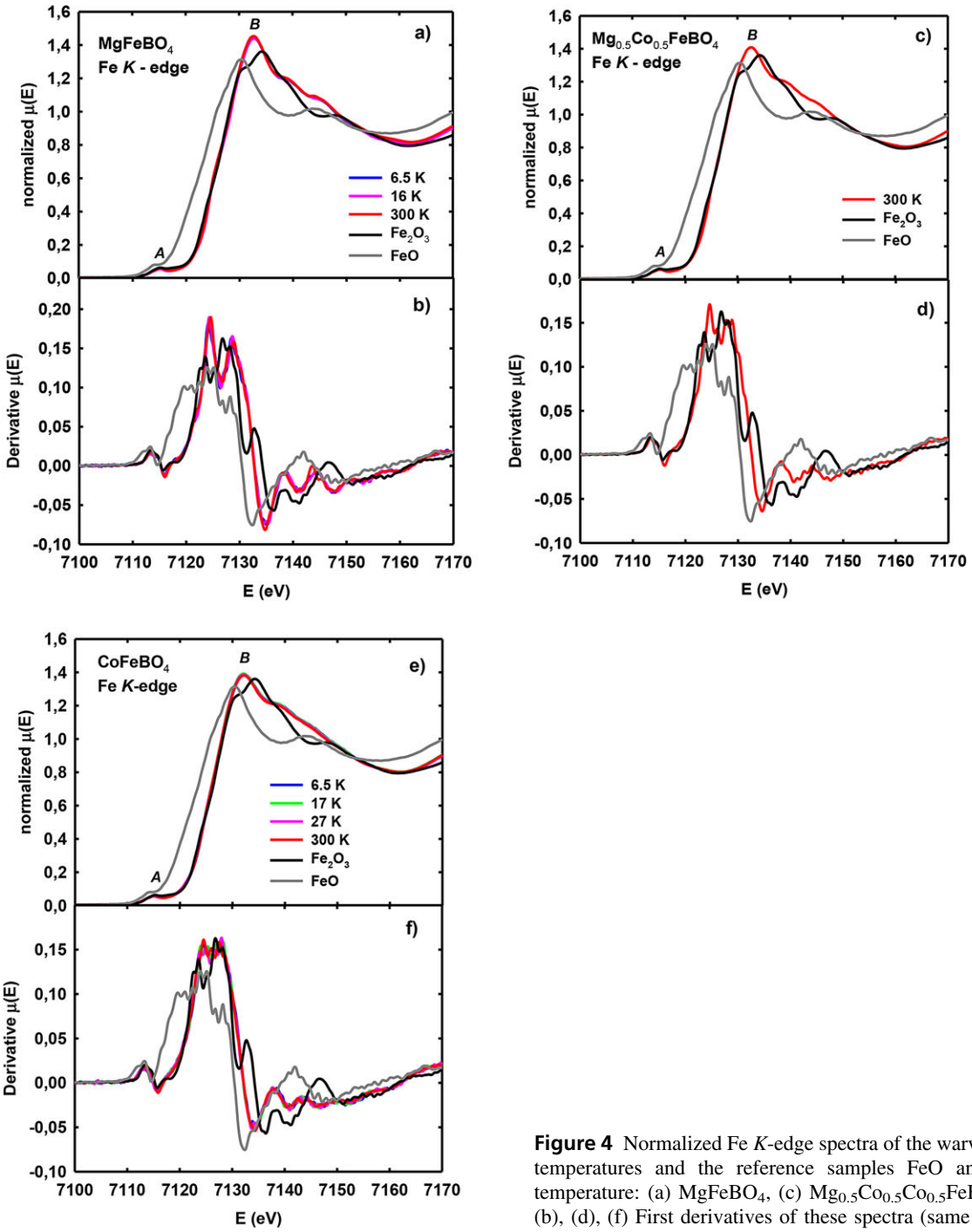

Figure 4 Normalized Fe *K*-edge spectra of the warwickites at different temperatures and the reference samples FeO and Fe_2O_3 at room temperature: (a) $MgFeBO_4$, (c) $Mg_{0.5}Co_{0.5}Co_{0.5}FeBO_4$, (e) $CoFeBO_4$. (b), (d), (f) First derivatives of these spectra (same colors).

the peak B at 7225 eV. This reflects the fact that the Co environment remains six-coordinate and distorted as the Co content increases. This conclusion is supported by the crystal-structure refinement where tetragonal distortion of both octahedra was clearly revealed.

3.2.2 EXAFS spectra According to the X-ray crystallographic data, the average MO_6 octahedron becomes smaller and progressively distorted with Co doping. We have examined Co substitution effects on the local structural distortion by analyzing the Co and Fe *K*-edge EXAFS spectra.

The EXAFS spectra of three orthorhombic warwickites were measured at various temperatures from 6.5 K up to 300 K. Figures 8 and 9 show the Fourier transforms (FT) of the EXAFS functions for $MgFeBO_4$, $Mg_{0.5}Co_{0.5}FeBO_4$, and $CoFeBO_4$ at the Fe and Co *K*-edges, respectively. Three main features can be observed. The first one is the peak at

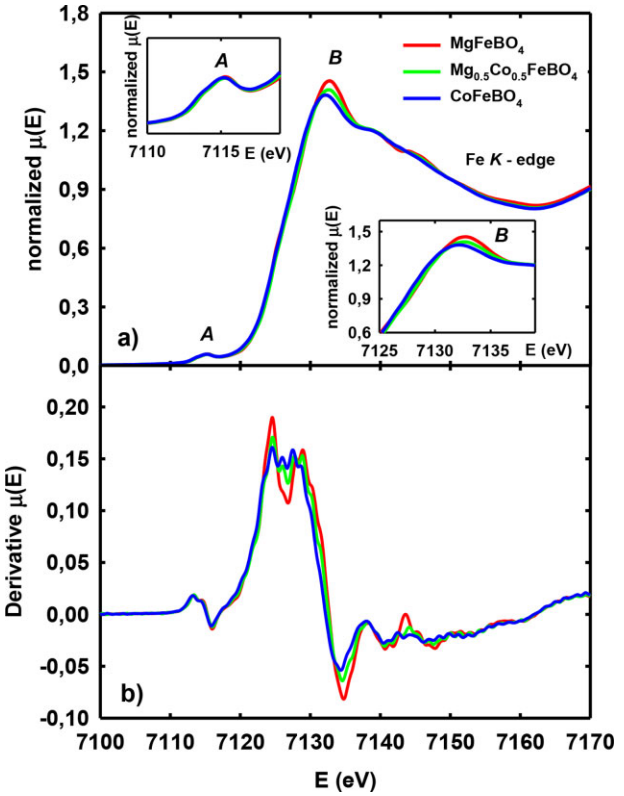

Figure 5 (a) Normalized Fe *K*-edge spectra of $MgFeBO_4$, $Mg_{0.5}Co_{0.5}FeBO_4$, and $CoFeBO_4$ at room temperature. Top inset: Co-content independent pre-edge peak. Bottom inset: the B peak intensity dependence on the Co content. (b) First derivatives of the spectra.

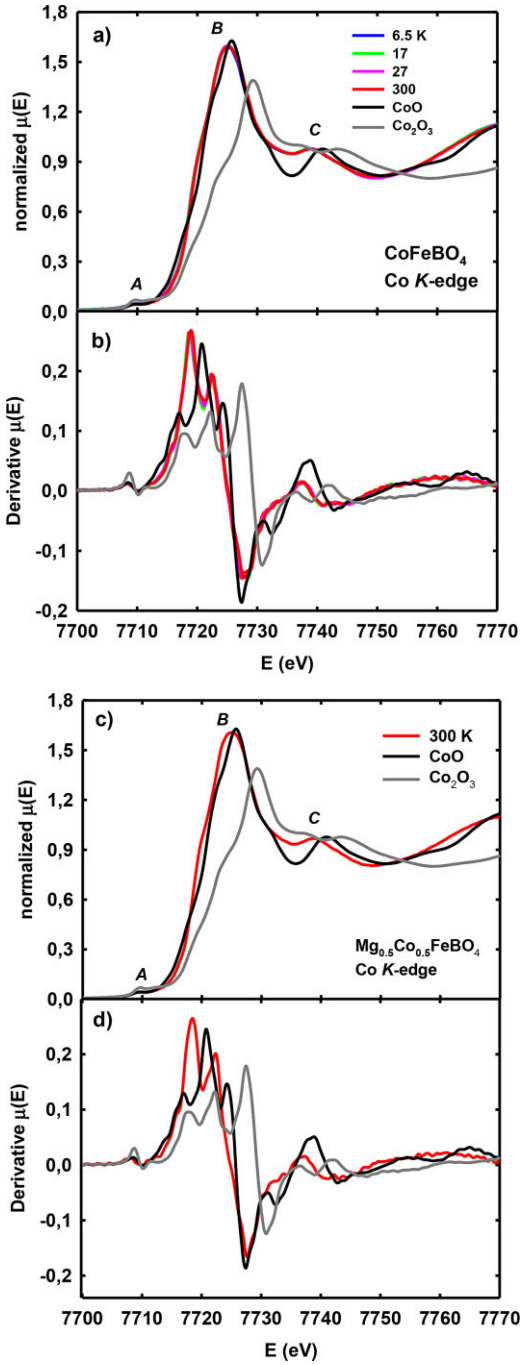

Figure 6 Normalized Co *K*-edge spectra of warwickites and the reference samples CoO and Co_2O_3 at room temperature: (a) $CoFeBO_4$, (c) $Mg_{0.5}Co_{0.5}FeBO_4$. (b), (d) First derivatives of these spectra (same colors).

about 1.5 Å corresponding to the first oxygen coordination shell Fe–O (Fig. 8). This single peak is split into two distinct peaks (a doublet) at ~1.28 and 1.61 Å corresponding to the first-shell Co–O bonds at the Co *K*-edge spectra (Fig. 9). The second feature between 2 and 3 Å is mainly related to the nearest metal neighbors (Fe, Co) along the M–O–M chains and the third one lies between 3 and 4 Å and includes contributions from the second-shell oxygen atoms (M–O) mainly. Peaks observed at even longer distances correspond to contributions from higher shell neighbors.

The temperature evolution of the Fe *K*-edge EXAFS spectra for the two end warwickites is presented in Fig. 8a and c. Both samples show a decrease in the first peak height as temperature increases. A similar trend is observed for the second peak. The intensity of the first coordination shell peak decreases more progressively for $CoFeBO_4$ in comparison with that for $MgFeBO_4$. The second peak for $CoFeBO_4$ becomes less asymmetric as temperature increases. The weak temperature dependence of the intensity of the first oxygen shell found for $MgFeBO_4$ may indicate a nearly constant distortion of the FeO_6 octahedra within the temperature range studied. Moreover, the intensity decrease of the first oxygen shell peak is more pronounced as the Co content increases. This can be seen from the comparison of $MgFeBO_4$ and $CoFeBO_4$ FTs at room temperature (Fig. 10a). The intensity of the first shell is smaller for the $CoFeBO_4$. This fact indicates a more distorted local structure around the Fe atom for this compound.

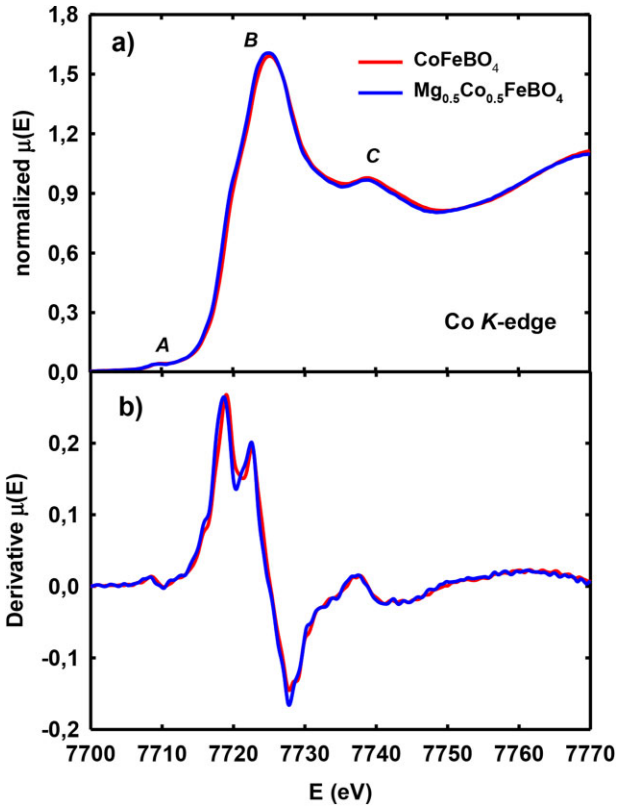

Figure 7 (a) Normalized Co *K*-edge spectra of $Mg_{0.5}Co_{0.5}FeBO_4$ and $CoFeBO_4$ at room temperature showing no dependence of XANES spectra on the Co content. (b) First derivatives of these spectra (same colors).

The temperature dependence of the EXAFS spectra at the Co *K*-edge has shown that the intensity of the doublet corresponding to the first oxygen shell Co–O for $CoFeBO_4$ significantly decreases with increasing tempera ture, indicating the distortion of the coordinated octahedra around the Co ion (Fig. 9b). The second peak demonstrates a similar temperature dependence. The comparison of room-temperature FT modulus of Co *K*-edge EXAFS spectra for $Mg_{0.5}Co_{0.5}FeBO_4$ and $CoFeBO_4$ is presented in Fig. 10b. The radial distribution function demonstrates that the asymmetric single peak with a wide shoulder corresponding to the first-shell Co–O bonds of $Mg_{0.5}Co_{0.5}FeBO_4$ is gradually split into two distinct peaks (a doublet) with increasing Co-doping content. This indicates a gradual increase in the local structural distortion of the CoO_6 octahedron with the Co substitution.

The main results of the quantitative structural analysis for the first coordination shell of the warwickites are summarized in Table S3 of Supporting Information (Crystal and local atomic structure of Co-doped MgFeBO4 warwickites) and in Fig. 11. The amplitude reduction factor S_0^2 was fixed to 0.85. The variables in the fits were the interatomic distances R_{M-O} and Debye–Waller (DW) factor σ^2. For each sample fits at different temperatures were performed with a fixed value of the threshold energy

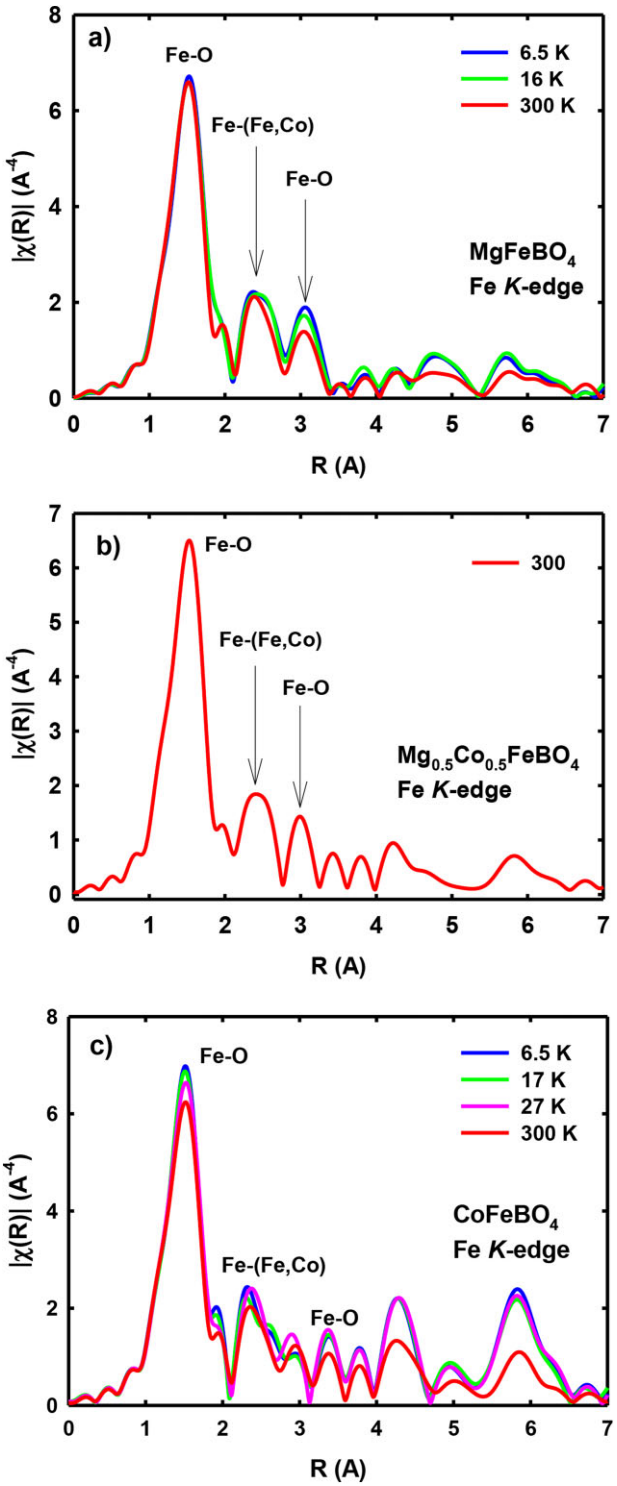

Figure 8 FT modulus of the k^3-weighted EXAFS spectra of the warwickites at the Fe *K*-edge as a function of temperature: (a) $MgFeBO_4$, (b) $Mg_{0.5}Co_{0.5}FeBO_4$, (c) $CoFeBO_4$.

$E_0 = 2$ eV obtained from the fit at the lowest temperature. The comparison between best fit and experimental spectra in term of the FT modulus of the k^3-weighted EXAFS signals and the real part of the Fourier-filtered spectra in *k*-space for

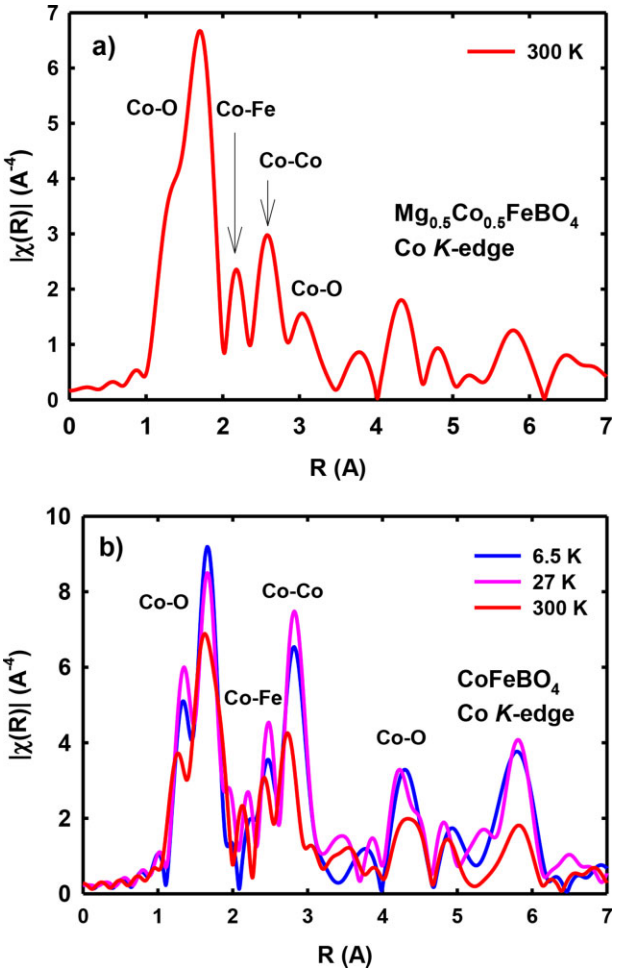

Figure 9 FT modulus of the k^3-weighted EXAFS spectra of the warwickites at the Co *K*-edge as a function of temperature: (a) $Mg_{0.5}Co_{0.5}FeBO_4$, (b) $CoFeBO_4$.

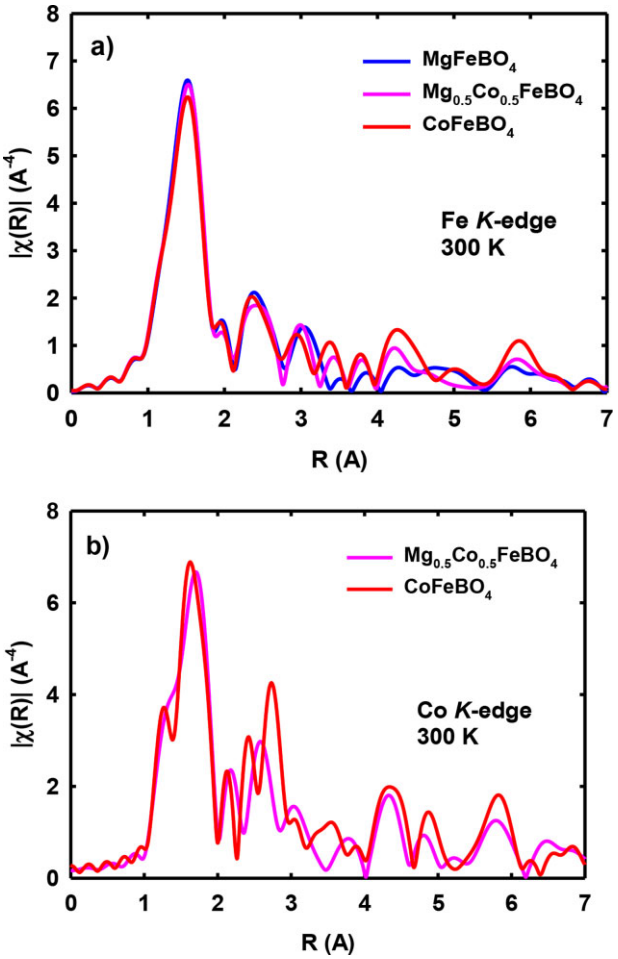

Figure 10 The room temperature FT modulus of the k^3-weighted EXAFS spectra of the $MgFeBO_4$, $Mg_{0.5}Co_{0.5}FeBO_4$, and $CoFeBO_4$: (a) Fe *K*-edge, (b) Co *K*-edge.

$CoFeBO_4$ are shown in Fig. S1. Similar agreements were found for the other warwickites. We have adopted the orthorhombic crystallographic structure at high temperature to calculate theoretical amplitudes and phases for each scattering path up to 7.0 Å, including the first Fe,Co–O coordination shell. We have been able to distinguish four short R^{short} and two long R^{long} (Fe,Co–O) bonds.The temperature dependence of the average Fe–O, Co–O interatomic distances and its DW factors are compared in Fig. 11a and b, respectively. Both Fe–O and Co–O average inter-atomic distances show no dependence on the Co content. The average Fe–O distance in both $MgFeBO_4$ and $CoFeBO_4$ remains almost constant in the whole temperature range within the experimental error. For $MgFeBO_4$, the DW factor of the average Fe–O distance does not show strong changes with decreasing temperature. These results indicate that the local distortion of the FeO_6 octahedra in $MgFeBO_4$ is almost temperature independent over the whole temperature range. By contrast, a rather pronounced temperature dependence of the DW factor of the average Fe–O distances was found for $CoFeBO_4$ below 27 K. In fact, in recent magnetization measurements, a spin-glass magnetic transition has been found at 22 K [22]. The freezing of the magnetic fluctuations of the Fe^{3+} magnetic moments below the spin-glass transition was observed in temperature-dependent experiments [23]. It is conjectured that the reduction of these fluctuations may have an influence in the decrease of the DW factor by magnetoelastic interaction. The DW factor of each scattering path includes contributions from both thermal vibrations and local distortions. The thermal vibration contribution decreases upon cooling. A large DW factor obtained for the high-temperature phase indicates that the local environment around the Fe atom is locally distorted, with the dynamical contribution prevailing. The DW factor of the Co–O first shell distances shows weak variation with temperature. The value of σ^2 factor increases for both average distances Fe–O and Co–O with Co content. Thus, the Co addition induces an increase in the local structure distortion of both FeO_6 and CoO_6 octahedra.

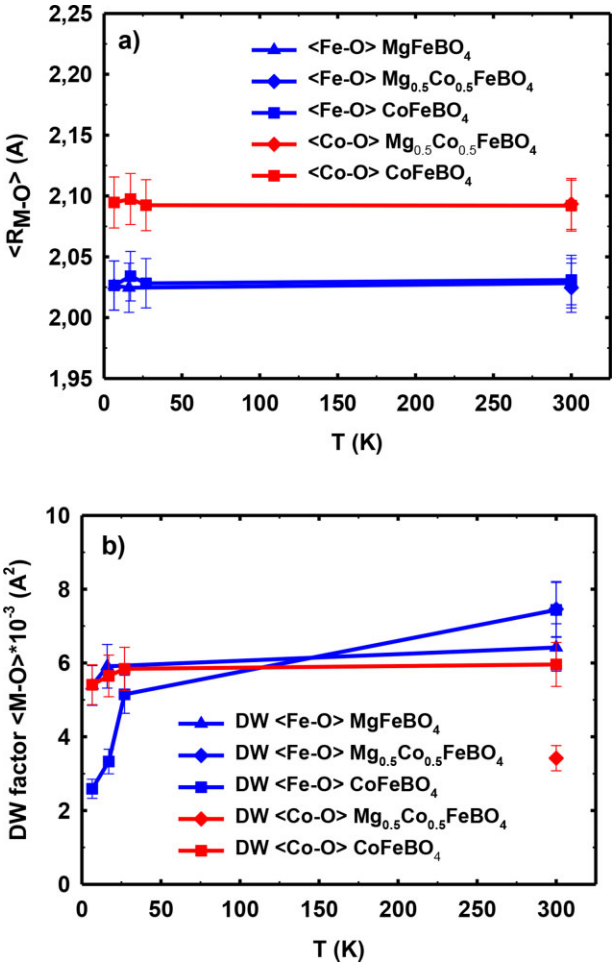

Figure 11 Temperature dependences of (a) average interatomic Fe–O and Co–O distances and (b) DW factors for the average Fe–O and Co–O distances.

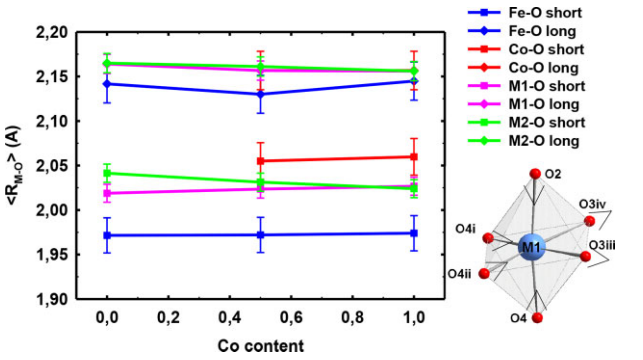

Figure 12 The variation of the two distinct average bond distances M–O with Co content obtained from X-ray crystallographic and EXAFS analysis. $T = 300$ K. A sketch of the $M1O_6$ octahedra with the arrows indicating the distortion from ideal octahedron is shown.

The EXAFS spectra are very useful to distinguish between individual contributions of each type of surrounding atoms that otherwise are overlapped in the X-ray crystallographic data. The warwickite structure has Mg, Co, and Fe atoms distributed over two nonequivalent local environments. According to Shannon [43], average Fe–O bond lengths 2.14 and 2.02 Å, respectively, are expected for octahedrally coordinated Fe^{2+} and Fe^{3+} ions. The average Fe–O bond distance of the FeO_6 octahedra deduced from EXAFS data is ~2.03 Å, strongly implying purely trivalent state of the iron ions. A larger value of the average Co–O distance as compared to the Fe–O one is obtained for both $Mg_{0.5}Co_{0.5}FeBO_4$and $CoFeBO_4$. This increase is correlated with the decrease in the formal valence state of the octahedral Co ion, namely, Co^{2+} instead Fe^{3+}. The average Co–O bond lengths for both Co warwickites (~2.10 Å) are close to 2.09 Å expected for the octahedrally coordinated Co^{2+} ion [43]. So, from the EXAFS study, we conclude that iron and cobalt enter into the warwickite structure in the trivalent and divalent states, respectively. The Co^{2+} atoms with larger ionic radii ($r_i = 0.72$ Å) replace the Fe^{3+} ones ($r_i = 0.645$ Å) at the octahedral M1 site thus increasing the average M1–O bond lengths. This increase is correlated with the shortening of average M2–O bonds suggesting that Fe^{3+} ions move to the M2 octahedral site. The fact that Co atoms could replace Fe ones at the octahedral site in $CoFeBO_4$ would induce an apparent increase of the DW factor.

The variation of the two distinct distances as a function of Co-doping content obtained from the structural refinement and from the EXAFS study is presented in Fig. 12. Two oxygen ions are located at a distance of $R^{long}_{Fe-O} = R^{long}_{Co-O} = 2.14-2.16$ Å forming "long bonds" that approach the value of the long bond $R^{long}_{M-O} = 2.15-2.16$ Å given for the orthorhombic structure from diffraction studies. The four remaining oxygen ions are at the average distances of $R^{short}_{Fe-O} = 1.97$ Å and $R^{short}_{Co-O} = 2.06$ Å belonging to the "short bonds". These distances are close but a little different than the average short crystallographic distance $R^{short}_{M-O} = 2.03$ Å. In short, first, the EXAFS results have revealed that the refined structure, thus, arises from averaging local structures for each type of ions, Fe or Co. Secondly, the M–O bond anisotropy (e.g., the difference in the bond distances between the long and short M–O bond lengths) has been found to be in accordance with the crystallographic data.

The Co addition gives rise to the distortions of the coordination octahedra as mentioned above. Namely, the Co addition is accompanied by shifts in the oxygen positions and causes the increase in the bond lengths along the *c*-axis (rhombic distortions) and decrease in the perpendicular direction (tetragonal ones), as seen from the normal coordinates Q_2 and Q_3. The largest distortion is a compression perpendicular to the *c*-axis as seen from the planar and the axial average radii. The observed increase in Q_3 for M2 site can assign to FeO_6 octahedra with short axial bonds ~1.97 Å. As the Co content increases, the rhombic distortions increase for the M1 site. The substitution of the isotropic Fe^{3+} (d^5) by Co^{2+} (d^7) at the M1 sites introduces

two extra electrons. Taking into account spin–orbit coupling Co^{2+} in the distorted oxygen octahedra is described by two Kramers doublets separated by approximately 100 K. It is known that the magnetocrystaline anisotropy depends on the actual distortion and also on the charge differences beyond the first coordination [44]. Therefore, an induced anisotropy by Co substitution is expected. Indeed, in Ref. [22], we show that as Co is introduced first in the $Mg_{0.5}Co_{0.5}FeBO_4$, the induced anisotropy is along the *a* crystal axis, while in the fully substituted $CoFeBO_4$, it is along the *b*-axis. The striking magnetic anisotropy properties have been observed in the parent ludwigites [45, 46]. The Co^{2+} ions push the Fe^{3+} ones from the M1 site ($V_{zz} = 0.104\, e\text{Å}^3$) to the M2 one ($V_{zz} = 0.087\, e\text{Å}^3$), for which the t_{2g} orbitals splitting should be smaller.

4 Conclusions In the present work, a careful study of the electronic state, long-range, and local structural properties of three-component warwickite system $Mg_{1-x}Co_xFeBO_4$ has been carried out. XANES/EXAFS spectra analysis is supported by X-ray crystallographic data to build up a wide view of the electronic state and local structure of metal ions.

The X-ray diffraction and XANES analysis in this work have shown unambiguously that Mg and Co enter into the warwickite structure in divalent state, while Fe enters in the trivalent state. Those experiments also show the existence of some preferential occupation habits of Fe^{3+}. In fact, the information on the occupation probabilities of the two sites can be complemented by the partial information on their occupation by the Fe atoms, provided by Mössbauer spectroscopy (MS) (see Table 4) [23]. In $MgFeBO_4$, there is qualitative agreement since both techniques indicate that Fe^{3+} enters mostly at the M1 site, while in $CoFeBO_4$, MS spectra analysis shows that Fe^{3+} sits with a larger probability at the M2 sites. Low-symmetric Jahn–Teller-like distortions exist for both coordinated octahedra as can be seen from the normal coordinates calculations. As the Co content increases, the structural distortions become more pronounced. An alternation of the octahedra principal axes within the ribbon was found.

The XRD data yield the average M–O distances over the two metal Fe and Co, so the increasing distortion cannot be assigned either to Fe or Co atoms. In spite of this, the V_{zz} calculated with those data increases with Co content and shows that Co atoms plays an important role in the structure modification. The effect of Co substitution is clarified by means of the element selective techniques XANES and EXAFS data.The average interatomic distances Fe–O and Co–O provide direct evidence for trivalent and divalent states of iron and cobalt ions, respectively. The electronic states of the Fe and Co are not affected by the substitution. The substituted Co ions have two roles: one is pushing the Fe atom from M1 site to M2 site, which is expressed in the reduction of the M2 site volume, and the other is an increase in the local distortions in FeO_6 and CoO_6 octahedra. In addition to XRD data, EXAFS analysis revealed that the Fe–O short bonds are smaller than the Co–O ones. So, the tetragonal distortions are expected to be greater for FeO_6 octahedra than for CoO_6 ones. At the same time, the substitution of Fe^{3+} ions by Co^{2+} ions at the M1 site induces an increase in the rhombic distortion of $M1O_6$ octahedra.

Finally, we may infer that the local structure distortions around the magnetic Fe and Co atoms could play an important role in magnetic properties and in magnetic crystalline anisotropy, especially. The magnetic properties of the $Mg_{1-x}Co_xFeBO_4$ warwickite system will a matter of future study.

Supporting Information

Additional supporting information may be found in the online version of this article at the publisher's website.

Acknowledgments This work has been financed by the MECOM Project MAT11/23791, and DGA IMANA project E-34, Council for Grants of the President of the Russian Federation (project nos. NSh-2886.2014.2, SP-938.2015.5), and Russian Foundation for Basic Research (project nos. 13-02-00958-a, 13-02-00358-a, 14-02-31051-mol-a). The work of one of the coauthors (M.S.P.) was supported by the program of Foundation for promoting the development of small enterprises in scientific and technical sphere ("UMNIK" program).

References

[1] K. Seleznyova, M. Strugatsky, S. Yagupov, N. Postivey, A. Artemenko, and J. Kliava, Phys. Status Solidi B **251**, 1393 (2014).
[2] V. E. Dmitrienko, E. N. Ovchinnikova, S. P. Collins, G. Nisbet, G. Beutier, Y. O. Kvashnin, V. V. Mazurenko, A. I. Lichtenstein, and M. I. Katsnelson, Nature Phys. **10**, 202 (2014).
[3] D. Afanasiev, I. Razdolski, K. M. Skibinsky, D. Bolotin, S. V. Yagupov, M. B. Strugatsky, A. Kirilyuk, Th. Rasing, and A. V. Kimel, Phys. Rev. Lett. **112** (1), 147403 (2014).
[4] K. Kumari, K. K. Bhargav, N. Kumar, S. Ram, and R. K. Kotnala, Phys. Status Solidi A **208**, 2130 (2011).
[5] Sh. Li, J. Leng, Ya. Fan, Ch. Fu, H. Shen, Y. Xue, and D. Xu, Phys. Status Solidi A **208**, 114 (2011).
[6] M. Matos, J. Terra, D. E. Ellis, and A. S. Pimentel, J. Magn. Magn. Mater. **374**, 148 (2015).
[7] R. Bubnova and S. Filatov, Phys. Status Solidi B **245**, 2469 (2008).
[8] I. A. Troyan, A. G. Gavrilyuk, S. G. Ovchinnikov, I. S. Lyubutin, and N. V. Kazak, JETP Lett. **94**, 748 (2011).
[9] A. Akpar, M. Angst, P. Khalifah, D. Mandrus, B. C. Sales, and L. Forro, Phys. Rev. B **82**, 165106 (2010).
[10] T. G. Rappoport, L. Ghivelder, J. C. Fernandes, R. B. Guimarães, and M. A. Continentino, Phys. Rev. B **75**, 054422 (2007).
[11] J. C. Fernandes, R. B. Guimãraes, M. A. Continentino, H. A. Borges, J. V. Valarelli, and A. Lacerda, Phys. Rev. B **50**, 16754 (1994).
[12] M. Brunner, J.-L. Tholence, L. Puech, S. Haan, J. J. Capponi, R. Calemczuk, J. C. Fernandes, and M. A. Continentino, Physica B **233**, 37 (1997).
[13] S. Yanez-Vilar, M. Sanchez-Andujar, J. Mira, S. Castro-Garcia, J. Rivas, and M. A. Senaris-Rodriguez, J. Appl. Phys. **108** (7), 074115 (2010).

[14] J. J. Capponi, J. Chenavas, and J. C. Joubert, J. Solid State Chem. **7**, 49 (1973).
[15] Z. Yang, X. L. Chen, J. K. Liang, Y. C. Lan, and T. Xu, J. Alloys Compd. **319**, 247 (2001).
[16] M. J. Buerger and V. Venkatakrishan, Mater. Res. Bull. **7**, 1201 (1972).
[17] J. J. Capponi, J. Chenavas, and J. C. Joubert, Mater. Res. Bull. **8**, 275 (1973).
[18] A. D. Balaev, O. A. Bayukov, A. D. Vasiliev, D. A. Velikanov, N. B. Ivanova, N. V. Kazak, S. G. Ovchinnikov, M. Abd-Elmeguid, and V. V. Rudenko, JETP **97**, 989 (2003).
[19] H. K. Li, G. M. Cai, J. J. Fan, and Z. P. Jin, J. Alloys Compd. **516**, 107 (2012).
[20] A. Apostolov, M. Mikhov, and P. Toholakov, Phys. Status Solidi A **56**, K33 (1979).
[21] R. B. Guimarães, J. C. Fernandes, M. A. Continentino, H. A. Borges, C. S. Moura, J. B. M. da Cunha, and C. A. dos Santos, Phys. Rev. B **56**, 292 (1997).
[22] A. Arauzo, N. V. Kazak, N. B. Ivanova, M. S. Platunov, Yu. V. Knyazev, O. A. Bayukov, L. N. Bezmaternykh, I. S. Lyubutin, K. V. Frolov, S. G. Ovchinnikov, and J. Bartolomé, J. Magn. Magn. Mater. **392**, 114 (2015).
[23] I. S. Lyubutin, N. Yu. Korotkov, K. V. Frolov, N. V. Kazak, M. S. Platunov, Yu. V. Knyazev, L. N. Bezmaternyh, S. G. Ovchinnikov, A. Arauzo, and J. Bartolomé, J. Alloys Compd. **642**, 204 (2015).
[24] Yu. V. Knyazev, N. V. Kazak, M. S. Platunov, N. B. Ivanova, L. N. Bezmaternykh, A. Arauzo, J. Bartolomé, and S. G. Ovchinnikov, J. Alloys Compd. **642**, 232 (2015).
[25] J. P. Attfield, A. M. T. Bell, L. M. Rodriguez-Martinez, J. M. Greneche, R. J. Cernik, J. F. Clarke, and D. A. Perkins, Nature **396**, 655–658 (1998).
[26] M. A. Continentino, A. M. Pedreira, R. B. Guimarães, M. Mir, J. C. Fernandes, R. S. Freitas, and L. Ghivelder, Phys. Rev. B **64**, 014406 (2001).
[27] G. R. Hearne, W. N. Sibanda, E. Carleschi, V. Pischedda, and J. P. Attfield, Phys. Rev. B **86**, 195134 (2012).
[28] B. Rivas-Murias, F. Rivadulla, M. Sánchez-Andújar, A. Castro-Couceiro, M. A. Señarís-Rodríguez, and J. Rivas, Chem. Mater. **18**, 4547 (2006).
[29] R. J. Goff, A. J. Williams, and J. P. Attfield, Phys. Rev. B **70**, 014426 (2004).
[30] J. P. Attfield, A. M. T. Bell, L. M. Rodriguez-Martinez, J. M. Greneche, R. Retoux, M. Leblanc, R. J. Cernik, J. F. Clarke, and D. A. Perkins, J. Mater. Chem. **9**, 205 (1999).
[31] N. V. Kazak, M. S. Platunov, Yu. V. Knyazev, N. B. Ivanova, O. A. Bayukov, A. D. Vasiliev, L. N. Bezmaternykh, V. I. Nizhankovskii, S. Yu. Gavrilkin, K. V. Lamonova, and S. G. Ovchinnikov, J. Magn. Magn. Mater. **393**, 316 (2015).
[32] M. Matos and R. B. Oliveira, J. Phys.: Condens. Matter **18**, 8267 (2006).
[33] M. S. Platunov, S. G. Ovchinnikov, N. V. Kazak, N. B. Ivanova, V. N. Zabluda, E. Weschke, E. Schierle, and K. V. Lamonova, JETP Lett. **96**, 650 (2013).
[34] N. V. Kazak, M. S. Platunov, N. B. Ivanova, Y. V. Knyazev, L. N. Bezmaternykh, E. V. Eremin, O. A. Bayukov, S. G. Ovchinnikov, D. A. Velikanov, and Y. V. Zubavichus, JETP **117**, 94 (2013).
[35] T. D. Kelly, L. Kong, D. A. Buchanan, A. T. Brant, J. C. Petrosky, J. W. McClory, V. T. Adamiv, Y. V. Burak, and P. A. Dowben, Phys. Status Solidi B **250**, 1376 (2013).
[36] G. M. Sheldrick, Acta Crystallogr. A **46**, 467 (1990).
[37] S. I. Zabinski, J. J. Rehr, A. Ankudinov, and R. C. Alber, Phys. Rev. B **52**, 2995 (1995).
[38] M. Newville, J. Synchrotron Radiat. **8**, 322 (2001).
[39] R. Norrestam, M. Kritikos, and A. Sjodin, J. Solid State Chem. **114**, 311 (1995).
[40] I. D. Brown and D. Altermatt, Acta Crystallogr. B **41**, 244 (1985).
[41] R. M. Wood and G. J. Palenik, Inorg. Chem. **37**, 4149 (1998).
[42] R. Norrestam, Z. Kristallogr. **189**, 1 (1989).
[43] R. D. Shannon, Acta Crystallogr. A **32**, 751 (1976).
[44] M. Tachiki, Prog. Theor. Phys. **23**, 1055 (1960).
[45] J. Bartolomé, A. Arauzo, N. V. Kazak, N. B. Ivanova, S. G. Ovchinnikov, Yu. V. Knyazev, and I. S. Lyubutin, Phys. Rev. B **83**, 144426 (2011).
[46] N. B. Ivanova, N. V. Kazak, Yu. V. Knyazev, D. A. Velikanov, L. N. Bezmaternykh, S. G. Ovchinnikov, A. D. Vasiliev, M. S. Platunov, J. Bartolomé, and G. S. Patrin, JETP **113**, 1015 (2011).

